Structure of the human CTF18 clamp loader bound to PCNA

Giuseppina R. Briola[1,*], Muhammad Tehseen[1,*], Amani Al-Amodi[1], Phong Quoc Nguyen[1], Christos G. Savva[1], Samir M. Hamdan[1] and Alfredo De Biasio[1]

[1]Bioscience Program, Division of Biological and Environmental Sciences and Engineering, King Abdullah University of Science and Technology, Thuwal 23955, Saudi Arabia.

Correspondence should be addressed to S.M.H. (samir.hamdan@kaust.edu.sa) or A.D.B. (alfredo.debiasio@kaust.edu.sa)

* These authors have contributed equally

Abstract

Sliding clamps like PCNA are crucial processivity factors for replicative polymerases, requiring specific clamp loaders for loading onto DNA. The clamp loader CTF18 interacts with the leading strand polymerase Pol ε and loads PCNA onto primer/template DNA using its RFC pentameric module. Here, we provide a structural characterization of the human CTF18 complex and its interaction with PCNA. Our cryo-EM data support that the Ctf8 and Dcc1 subunits of CTF18, which form the regulatory module interacting with Pol ε, are flexibly tethered to the RFC module. A 2.9 Å cryo-EM structure shows the RFC module bound to PCNA in an auto-inhibited conformation similar to the canonical RFC loader, marking the initial step of the clamp-loading reaction. The unique RFC1 large subunit of CTF18, which shows high relative mobility, is anchored to PCNA through an atypical low-affinity PIP box in the AAA+ domain and engages the RFC5 subunit using a

novel β-hairpin at the disordered N-terminus. These dual interactions may allow CTF18 RFC1 to outcompete the canonical RFC1 subunit while recycling the RFC2-3-4-5 subunits. Our results suggest that CTF18 comprises two structurally independent modules that cooperate in loading PCNA onto the leading strand for replication by Pol ε.

Introduction

High fidelity and efficiency are critical for chromosomal DNA duplication in eukaryotes. This precision is achieved through the coordinated action of replicative DNA polymerases, Pol δ and Pol ε, anchored to the sliding clamp, Proliferating Cell Nuclear Antigen (PCNA) [1]. The ring-shaped PCNA homotrimer encircles DNA, enhancing the processivity of these polymerases in DNA replication and repair processes, including excision repair and homologous recombination [2], and plays an important role in sister chromatid cohesion establishment [3]. The closed-ring topology of PCNA necessitates the transient opening of one interface to facilitate the incorporation and trapping of primer-template DNA. This critical function is executed by pentameric AAA+ ATPases, collectively known as clamp loaders [4-6]. Extensive structural and biochemical work in different organisms [7-12] established a common mechanism for the clamp-loading reaction, which proceeds through three main steps [13-18]. Initially, the clamp loader engages with the intact clamp ring, adopting an autoinhibited configuration that precludes DNA binding [10]. This stage sets the groundwork for the subsequent transition, where the clamp loader alters its conformation to an activated state. This change facilitates the opening of the clamp ring, creating a gap sufficiently large to permit the passage of duplex DNA and aligning the clamp loader for primer-template DNA interaction. The final phase of this process is

initiated by the binding of DNA to the clamp loader, catalyzing ATP hydrolysis. This action prompts the closure of the clamp and the concurrent disassembly of the clamp loader, completing the cycle necessary for the engagement of the replicative polymerases to start DNA synthesis.

The canonical Replication Factor C (RFC), consisting of a large RFC1 subunit and four smaller subunits (RFC2, RFC3, RFC4 and RFC5), acts as the primary clamp loader for PCNA [4, 19]. However, eukaryotes also employ alternative loaders [20], including CTF18 [6, 21-24], highlighting the specificity of loading mechanisms facilitating DNA replication fidelity and efficiency.

Genome-wide analyses revealed that CTF18 predominantly facilitates PCNA loading on the leading strand, in contrast to the canonical RFC complex, which mainly loads PCNA on the lagging strand [25]. Although CTF18 is not essential for bulk DNA replication in yeast [26, 27], it plays a vital role in ensuring sister chromatid cohesion [21, 28, 29]. This may be due to its selective loading of PCNA linked to EcoI acetyltransferase [3], which acetylates Smc3, preventing cohesin destabilization by WapI [30-32]. Recruitment of CTF18 to the leading strand is also important for activation of the replication checkpoint [22, 24, 33, 34].

The CTF18 complex features two distinct modules with separate functions [23, 35, 36]: a catalytic RFC module for PCNA loading, consisting of a large RFC1-like subunit (hereby referred to as Ctf18), alongside the four RFC2, RFC3, RFC4 and RFC5 subunits utilized by the canonical RFC complex, and a regulatory module, made up of the Ctf8 and Dcc1 subunits. These latter two subunits attach to the Ctf18 C-terminus, forming the Ctf18-1-8 module. A long linker predicted to be flexible connects the catalytic segment of

Ctf18 to its regulatory C-terminus. Structural and functional studies have demonstrated that the interaction between the Ctf18-1-8 module and the catalytic domain of Pol2 ($Pol2_{CAT}$), the principal subunit of Pol ε, directs CTF18 to replication forks and boosts its clamp loading efficiency [34, 37]. This interaction situates the clamp loader close to the primer/template junction, facilitating PCNA loading [34]. $Pol2_{CAT}$ is tethered to the remainder of Pol ε via an unstructured linker, making it an integral component of the CMGE (CMG-Pol ε) core replisome complex [38]. It has been proposed that Pol ε utilizes both the CMG helicase and PCNA as processivity factors to facilitate normal replication rates [39, 40]. Tethering by the CMG complex might allow Pol ε to dissociate from the 3′ end of the leading strand but stay at the replication fork until leading strand synthesis restarts. Given Pol ε relatively weak interaction with PCNA [41], it is possible that multiple PCNA loading events on the leading strand via CTF18 are necessary to achieve full Pol ε processivity.

Although the structure of the Ctf18-1-8 module in association with $Pol2_{CAT}$ has been elucidated [34, 37], the architecture of the CTF18 RFC module and its interaction with PCNA remain uncharacterized. To investigate the clamp loading mechanism employed by CTF18, we reconstituted the full human RFC18 complex with PCNA and determined its structure using cryo-electron microscopy (cryo-EM). Our cryo-EM data supports the prediction that the Ctf18-1-8 and RFC modules are flexibly tethered. The analysis yielded high-resolution reconstructions of the entire CTF18 RFC module bound to a closed PCNA ring. Although the overall architecture mirrors the autoinhibited state observed in the canonical RFC loader in complex with PCNA [10], distinctive features

within CTF18 were identified. These distinctions may offer insights into the specialized functional roles CTF18 plays in DNA replication.

Materials and Methods

Protein expression and purification

Preparation of CTF18

Ctf18-RFC2-5 Ctf8 DCC1 plasmid (named hereafter Ctf18-RFC) encoding all seven subunits in a single MultiBac™ expression plasmid was transformed into DH10MultiBac™ cells to make bacmid DNA. To prepare the baculovirus, bacmid DNA containing all subunits was transfected into Sf9 cells using FuGENE® HD (Promega) according to the manufacturer's instructions. This baculovirus prep was amplified twice to obtain a higher titer virus (P3 virus). The expression of Ctf18-RFC then proceeded by transfecting a 6 L Hi5 suspension culture at a density of 2×10^6 cells/ml with the P3 virus for 60-65 hours. Cells were collected by centrifugation at 5,500 xg for 10 minutes and re-suspended in lysis buffer [50 mM Tris-HCl (pH 7.5), 300 mM NaCl, 20 mM imidazole, 5 mM BME, 0.1% Nonidet P-40, 10% glycerol and one EDTA-free protease inhibitor cocktail tablet/50 mL]. All further steps were performed at 4° C. Cells were sonicated and debris was removed by centrifugation at 95,834 xg for 1 hr at 4 °C. The resultant supernatant was directly loaded onto a HisTrap HP 5 mL affinity column (Cytiva) pre-equilibrated with buffer A [50 mM Tris-HCl (pH 7.5), 300 mM NaCl, 20 mM imidazole, 5 mM BME and 10% glycerol]. After loading, the column was washed with 50 mL of buffer A and the bound fractions were eluted by gradient with 50 mL of buffer B [50 mM Tris-HCl (pH 7.5), 300 mM NaCl, 500 mM imidazole, 5 mM BME, and 10% glycerol]. The eluents were pooled and directly loaded onto Strept Trap XT 1 mL affinity column pre-equilibrated with buffer A [50 mM

Tris-HCl (pH 7.5), 300 mM NaCl, 5 mM BME and 10% glycerol]. After loading, the column was washed with 10 mL of buffer A, followed by step elution with buffer B [50 mM Tris-HCl (pH 7.5), 300 mM NaCl, 50 mM Biotin, 5 mM BME, and 10% glycerol]. Eluents were pooled and concentrated to 1 mL and loaded onto HiLoad 16/600 Superdex 200 pg pre-equilibrated with gel filtration buffer [50 mM Tris-HCl (pH 7.5), 200 mM NaCl, 1 mM DTT, and 10% glycerol]. Protein fractions were pooled in a total volume of 1.6 mL, flash frozen, and stored at -80°C.

Preparation of PCNA

To express PCNA BL21(DE3) *E. coli* cells were transformed with WT PCNA plasmid. The transformed cells were grown at 37°C in 2YT media supplemented with ampicillin to an OD600 of 1.2. The cell cultures were induced with 0.5 mM isopropyl-beta-D-1-thiogalactopyranoside (IPTG) and let them grow for 19 hours at 16°C. Cells were then harvested by centrifugation at 5500 xg for 10 minutes and then re-suspended in lysis buffer [50 mM Tris-HCl (pH 7.5), 750 mM NaCl, 20 mM imidazole, 5 mM BME, 0.2% Nonidet P-40, 1 mM PMSF, 5% glycerol and one EDTA-free protease inhibitor cocktail tablet/50 mL]. The cells were lysed with 2 mg/mL of lysozyme at 4°C for 30 minutes. Cells were sonicated and debris was removed by centrifugation at 22,040 xg for 20 minutes at 4°C. The cleared cell lysate was directly loaded onto a HisTrap HP 5 mL affinity column (Cytiva) pre-equilibrated with buffer A [50 mM Tris-HCl (pH 7.5), 500 mM NaCl, 20 mM imidazole, 5 mM BME and 5% glycerol]. The column was firstly washed with 50 mL of buffer A and then with 50 mL of buffer B containing low salt [50 mM Tris-HCl (pH 7.5), 100 mM NaCl, 500 mM imidazole, 5 mM BME, and 5% glycerol]. The eluents were pooled and directly loaded onto HiTrap Q HP 5 mL anion exchange column (GE Healthcare) pre-

equilibrated with buffer D [50 mM Tris-HCl (pH 7.5), 100 mM NaCl, 5 mM BME and 5% glycerol]. The column was washed with 50 mL of buffer D after loading, followed by elution of 50 mL gradient with buffer E [50 mM Tris-HCl (pH 7.5), 1 M NaCl, 5 mM BME, and 5% glycerol]. Eluents were pooled and concentrated to 1.5 mL and loaded onto HiLoad 16/600 Superdex 200 pg pre-equilibrated with gel filtration buffer [50 mM Tris-HCl (pH 7.5), 150 mM NaCl, 1 mM DTT, and 5% glycerol]. Protein fractions were pooled, flash-frozen, and stored at -80°C. All protein concentrations were calculated by measuring their absorbance at 280 nm using the extinction coefficients calculated from the amino acid composition (Ctf18-RFC: 216,360 M^{-1} cm^{-1}; PCNA: 47,790 M^{-1} cm^{-1}).

DNA substrates

For the primer/template substrates used in all the structures described here, 80 base pairs template strand 5'-TTTTTTTTTTTTTTTTTTTTTTTTTTTTTTTTTTTT TTTTGACTGCAC GAATTAAGCAATTCGTAATCATGG TCATAGCT-3' was annealed to a 39 base pairs primer containing a 3' dideoxy cytosine chain terminator 5'-AGCTATG ACCATGATTACGAATTGCTTAATTCGTGCAGT[ddC]-3' to form the P/T substrate. The strands were mixed in an equimolar ratio in the presence of 20 mM Tris pH 7.5 and 25 mM NaCl. The annealing reaction was performed by incubating the P/T at 92°C for 2 minutes followed by slow cooling to room temperature overnight. All oligonucleotides were purchased from IDT Integrated DNA Technologies.

Mass photometry

Solution-phase mass determination of CTF18 was performed using the TwoMP (Refeyn) mass photometer. Experimental data were obtained as mass photometry videos recorded for 60s using the AcquireMP v2.5 software (Refeyn) on precleaned slides.

Before analysis, a mass calibration was performed using protein standards spanning a mass range between 86 to 239 kDa. Each standard was diluted to 100 nM with PBS buffer. A linear mass calibration was obtained via fitting of Gaussian functions to the ratiometric contrast values of each standard using the DiscoverMP v2.5 software (Refeyn). Similarly, the CTF18 stock was diluted into PBS buffer to a final concentration of 50 nM, and mass photometry videos were recorded and analyzed with the DiscoverMP v2.5 software.

Cryo-EM grids preparation and data collection

For all the complexes, UltraAuFoil® R1.2/1.3 Au 300 grids were glow-discharged at 30 mA for 30 seconds on an EasyGlow glow-discharge unit. For the preparation of the complex without Mg-Acetate (first dataset), P/T DNA, ATP, Ctf18-RFC, and PCNA were mixed in order. The final concentrations were 5.6 μM P/T DNA, 0.2 mM ATP, 1.5 μM Ctf18-RFC, and 7.5 μM PCNA. The buffer this was performed in comprised 50 mM Tris-HCl pH 7.5, 200 mM NaCl, 1 mM DTT, and 0.5 mM ATP. 3 μL of the sample was applied to the grid, blotted for 2 s at blot force -5, and plunged frozen into liquid ethane using a Vitrobot Mark IV (FEI Thermo Fisher), which was set at 4°C and 100% humidity. For the preparation of Ctf18-RFC/PCNA/P-T DNA/ATP/Mg-Acetate complex (second dataset), the components P/T DNA, ATP, Mg-Acetate, Ctf18-RFC, and PCNA were mixed in order. The final concentrations were 5.6 μM P/T DNA, 0.2 mM ATP, 1.9 mg/mL Mg-Acetate, 1.5 μM Ctf18-RFC, and 7.5 μM PCNA. The buffer this was performed in comprised 50 mM Tris-HCl pH 7.5, 200 mM NaCl, 1 mM DTT, 0.5 mM ATP, and 5 mM Mg-Acetate. 3 μL of the sample was applied to the grid in the same way as above for data collection. Cryo-EM data for all the samples were collected on a Thermo Fisher Scientific Titan Krios G4

transmission electron microscope at KAUST. Electron micrographs for the first dataset (Ctf18-RFC-PCNA with ATP in the absence of Mg-Acetate), were collected using a Falcon 4i detector at a dose rate of 7.5 e^-/pix/sec for 5 seconds and a calibrated pixel size of 0.93 Å. Focusing was performed over a range between -2.7 μm and -1.5μm, in 0.3 μm intervals. Electron micrographs for the second dataset (Ctf18-RFC-PCNA with ATP and Mg-Acetate) were collected using a Falcon 4i detector at a dose rate of 8.02 e^-/pix/sec for 5 seconds and a calibrated pixel size of 0.93 Å. Focusing was performed over a range between -2.7 μm and -1.5 μm, in 0.3 μm intervals.

Cryo-EM image processing

Preprocessing of both datasets **Dataset 1** (Ctf18-RFC, ATP, primer/template DNA and PCNA) and **Dataset 2** (Ctf18-RFC, ATP, Mg^{2+}, primer/template DNA and PCNA) was performed as follows: the micrographs were corrected for beam-induced motion and then integrated using MotionCor2 [42]. All frames were retained and a patch alignment of 4x4 was used. CTFFIND-4.12 estimated Contrast Transfer Function (CTF) parameters for each micrograph [43]. Integrated movies were inspected with Relion-4.0 for further image processing (7906 movies for **Dataset 1**, and 6181 movies for **Dataset 2**) [44]. Particle picking was performed in automated mode using Topaz [45] for **Dataset 1**. Particle extraction was carried out from micrographs using a box size of 55 pixels (pixel size: 3.65 Å/pixel). An initial dataset of 2 x 10^6 particles was cleaned by 2D classification followed by 3D classification with alignment. Three 3D classes were generated with populations of 31, 28, and 40%. 3D refinement, CtfRefine, and polishing were performed on the selected 3D classes corresponding to populations 31 and 40%. A bigger box size, 480 pixels (pixel

size: 0.93 Å/pixel) was used to re-extract the particles. 3D refinement, CtfRefine, and polishing yielded reconstruction at 2.9 Å.

Particle picking was performed in reference-based mode for **Dataset 2**. Particle extraction was carried out from micrographs using a box size of 55 pixels (pixel size of 3.65 Å/pixel). An initial dataset of 3 x 10^6 particles was cleaned by 2D classification followed by 3D classification with alignment. Three 3D classes were generated with 30, 33, and 36% populations. 3D refinement, CtfRefine, and polishing were performed on the selected 3D classes corresponding to populations 33 and 36%. 3D refinement, CtfRefine, and polishing yielded reconstruction at 3.3 Å.

Molecular Modelling

The structure of the Ctf18 large subunit of human CTF18 (Q8WVB6, residues 277-805) was generated with Phyre2 [46], using as a template the sequence of human RFC1 (P35251, residues 581-1034). The Ctf18 subunit model was then aligned to the RFC1 subunit in the structure of the human RFC clamp loader bound to PCNA in an autoinhibited conformation (PDB 6VVO, [10]) using Chimera, the RFC1 subunit was deleted, and the resulting model including Ctf18, subunits RFC2/3/4/5 and PCNA was rigid-body fitted into the cryo-EM map. The model was edited and real-space refined with Coot [47] following flexible fitting performed with ISOLDE [48]. A final real-space refinement was performed in Phenix [49], applying secondary structure constraints. The models of both CTF18–PCNA complexes with and without the Mg^{2+} ion were generated similarly.

Results

Structure of the human CTF18–PCNA complex

We employed single-particle cryo-EM to determine the structure of human CTF18 bound to PCNA. To this purpose, the full CTF18 complex, including Ctf18-1-8, was expressed in insect cells and purified to homogeneity (Supplementary Figure 1). The purified complex contains all subunits and exhibits a mass which approximates the expected value, as confirmed by mass photometry (Supplementary Figure 2). To trap CTF18 in different steps of the clamp loading reaction, the complex was vitrified in the presence of ATP, PCNA, and primer/template DNA but omitting the Mg^{2+} cofactor to halt hydrolysis, and then imaged by cryo-EM (Supplementary Figure 3). Surprisingly, image processing yielded only a major 3D class which included the CTF18 RFC pentamer bound to a closed PCNA ring (Supplementary Figure 4, Figure 1a-b), with no evidence of DNA density. The Ctf18-1-8 module, which is connected to the RFC module by a ~90 amino acid linker (Figure 1a), is not resolved in the map (Figure 1b), suggesting it is flexibly tethered to the RFC module. The map was refined to a global resolution of 2.9 Å (Supplementary Figure 4), which allowed the model building of the Ctf18 and the five RFC2, RFC3, RFC4 and RFC5 subunits as well as the PCNA homotrimer (Figure 1c). The final model refines to a map-to-model FSC of 3.0 Å at 0.5 threshold, with good refinement statistics (Supplementary Table 1).

The five CTF18-RFC subunits are positioned on top of the closed PCNA ring, which is planar and undistorted (Figure 1c). A structural comparison shows that the CTF18 RFC pentamer was trapped in an autoinhibited conformation analogous to that reported for the canonical human (h) and yeast (sc) RFC [8, 10], pertaining to the initial

step of the clamp loading reaction, right before clamp opening (Figure 1c). In such conformation, the AAA+ domains form an inactive, asymmetric spiral that is incompatible with DNA binding [8, 10]. The AAA+, collar, and A' domains of the Ctf18 subunit (Figure 2a) align to the homologous domains of hRFC1 (Figure 2b); as in the hRFC structure [10], this subunit interacts with subunits RFC2 and RFC3 as well as PCNA (Figure 2c). Three main deviations from the hRFC–PCNA structure are observed [10]: a different tilt of the PCNA ring (Figure 1b-c), significant mobility of the large (Ctf18) subunit (Figure 1b and Supplementary Figure 5) and, importantly, the presence of a β-hairpin engaged to the outer surface of the RFC5 subunit, which we mapped to the disordered N-terminus of the Ctf18 subunit (Figure 2a and 2c). These features are analyzed in detail below.

Structure of the large subunit of CTF18

The Ctf18 subunit presents 22% identity with the homologous subunit RFC1 of hRFC and an overall structural conservation, with some deviations particularly in the A' domain (Figure 2a-b). Compared to the RFC2/3/4/5 subunits, the AAA+ domain of Ctf18 shows increased flexibility, as evidenced by the local resolution map of the complex (Supplementary Figure 4). The C-terminal region predicted to interact with the Ctf8 and Dcc1 subunits (Figure 2a) is invisible in the map. The most striking feature is a small β-hairpin-containing fold mapped between residues 165-194 in the disordered N-terminus (Figure 2a and 2c), ~80 Å apart from the Ctf18 AAA+ domain, to which it is connected by a disordered linker of 86 amino acids (residues 195-280). This N-terminal fold plugs into a groove at the outer surface of the collar domain of the RFC5 subunit (Figure 3a). The resolution of the map in this region is sufficient for confident model building of the interface (Figure 3b). The interface buries 984 $Å^2$ and is characterized by both apolar and polar

interactions (Figure 3a). A set of hydrophobic side chains protruding from one face of the Ctf18 β-hairpin (V178, V180, L190, L192) approach a complementary patch of hydrophobic residues on RFC3 (L255, N256, V291, F293, I336). The interface is further strengthened by several hydrogen bonds mostly mediated by main-chain atoms in the Ctf18 β-hairpin, and by a salt bridge between R193 of Ctf18 and D292 of RFC3 (Figure 3a).

Similarly to human Ctf18, long regions predicted to be disordered by AlphaFold [50] are present in the N-terminal sequence of Ctf18 of lower eukaryotes. While the β-hairpin region of human Ctf18 does not show strict sequence conservation, a similar fold in the N-terminus of *S.cerevisiae* and *Drosophila* Ctf18 is predicted (Figure 2a). Therefore, lower eukaryotes may use similar β-hairpin motifs to bind the corresponding RFC5 subunit of the RFC-module complex.

Interactions of CTF18 with PCNA

CTF18 engages two of the three PCNA protomers through four contact points involving the AAA+ domains of Ctf18, RFC2, RFC4 and RFC5 (Figure 1c and Figure 3c). The interactions with Ctf18, RFC2 and RFC5 subunits are analogous to those reported in the hRFC–PCNA complex [10]. However, while Ctf18 engages PCNA1 via a PIP-box interaction as hRFC1 [10], its atypical PIP motif lacking aromatic residues (Figure 2a, Figure 3d) results in a smaller buried surface area (763 vs 1010 $Å^2$). This low-affinity interaction may enhance the relative flexibility of the AAA+ domain of Ctf18 (Supplementary Figure 5). Differently from the hRFC–PCNA complex, where RFC4 is detached from PCNA [10], in CTF18 this subunit interacts with the Interdomain Connecting Loop (IDCL) of PCNA2 similarly as RFC2 binds PCNA1 (Figure 3d). The

RFC4–PCNA interaction, which was also observed in the structure of scRFC bound to an open PCNA [11], brings PCNA closer to the CTF18-RFC module, explaining the different tilt compared to the hRFC–PCNA complex (Figure 1c-d). Given the structure of scRFC bound to open PCNA [11], where all five RFC subunits are bound to PCNA (Figure 3c), we predict that a conformational shift in CTF18–RFC, specifically bringing the fifth subunit (RFC3) to engage PCNA3, would be necessary to disrupt the interface between PCNA3 and PCNA1, thereby opening the clamp and aligning the RFC subunits for primer-template DNA interaction. The reason for the absence of such an active CTF18 conformation in our cryo-EM analysis remains uncertain. However, similar to observations with the hRFC–PCNA complex, where an open-clamp state was not reported [10], this could be attributed to the hydrophobic regions of the open clamp interacting with the water-air interface, potentially leading to protein denaturation.

Nucleotide binding to the AAA+ modules

The map is consistent with nucleotides present in four of the five AAA+ domains of the CTF18 subunits (Figure 4a). ATP is bound to subunits Ctf18, RFC2 and RFC5, while ADP appears to engage RFC3, consistent with the structure hRFC–PCNA complex reconstituted with ATPγS [10]. Density for the adenine ring of ATP in the Ctf18 subunit is poor (Figure 4a), likely a consequence of the increased mobility of the AAA+ domain of this subunit (Supplementary Figure 5). Since RFC3 lacks critical catalytic residues [10], the presence of ADP, rather than a product of ATP hydrolysis, probably results from co-purification of the complex where ADP contaminants are present. In the human RFC complex, it has been previously shown that an intact nucleotide binding site in RFC3 has an important structural role in the complex assembly [51, 52]. If this is the case for CTF18

remains to be established, but it is likely that ADP binding to this subunit may be general and play a stabilizing role in all RFC-like loaders.

Differently from the hRFC–PCNA complex, where RFC4 is bound to ATPγS, in CTF18, this subunit is not engaged with a nucleotide (Figure 4a). The residues in the AAA+ of RFC4 of CTF18 that are coordinated to ATPγS in hRFC are displaced and not compatible with nucleotide binding. Interestingly, mutation of the conserved K84 residue in the ATP-binding motif of RFC4 in hRFC did not impair the ability of this subunit to assemble with other RFC subunits [52]. In agreement, our structure shows that the lack of ATP binding to RFC4 does not preclude the assembly of the CTF18 RFC pentamer in the autoinhibited conformation. However, considering the importance of ATP binding of RFC4 for the hRFC clamp loading function [51-53], it is expected that ATP binding to RFC4 in CTF18 is required for the switch to a conformation that is enzymatically active.

The asymmetric spiral of the CTF18 AAA+ pentamer (Figure 4a-b) disrupts the active sites at the RFC2/5 and RFC4/5 interfaces (Figure 4c). These disruptions, critical for the clamp-loading activity of eukaryotic RFCs, result from the loss of interactions with the trans-acting arginine fingers (Figure 4c). Additionally, the active site between Ctf18 and RFC2 is also disrupted (Figure 4c). However, prior research has indicated that this particular site is not essential for clamp loading by various loaders [54-56].

In CTF18, the AAA+ spiral is overtwisted in a manner reminiscent of the autoinhibited conformations observed in hRFC and scRFC [8, 10] (Figure 1c), leading to steric hindrance that impedes DNA binding (Figure 4a-b). Specifically, the overtwisted RFC3 and RFC4 subunits occupy the space normally filled by DNA. In the autoinhibited structure of hRFC, a β-hairpin (residues 68-88) located at the base of RFC3, also referred

to as "E-plug", extends towards the anticipated location of DNA and interacts with the Rossmann fold of RFC1 [10]. Conversely, in CTF18, while this same β-hairpin is oriented toward the interior of the DNA-binding channel (Figure 4d), it does not make direct contact with the Ctf18 subunit.

To discount the possibility that the absence of the Mg^{2+} ion in the cryo-EM sample could have hindered the proper assembly of the CTF18 AAA+ pentamer for DNA engagement, we used cryo-EM to visualize CTF18 with PCNA, primer-template DNA, ATP, and Mg^{2+} (Supplementary Figure 5; Supplementary Table 1). Despite the inclusion of Mg^{2+}, the resulting 3.3 Å reconstruction of the complex remained in a configuration analogous to that without Mg^{2+} (Figure 5a-b; Supplementary Figure 7). In this reconstruction, distinct density for Mg^{2+} is noted in the active sites of RFC2 and RFC5, coordinating ATP (Figure 5b). Similar to the map without Mg^{2+}, ADP coordination is present in RFC3, with an absence of nucleotide in RFC4. These findings collectively imply that the presence of Mg^{2+} in the pentamer active sites does not influence the transition of CTF18 from an autoinhibited to an active state. This result also confirms the remarkable stability of the autoinhibited conformation, even in hydrolyzing conditions.

Discussion

In this work, we reported the structure of the human CTF18 clamp loader bound to PCNA. Our cryo-EM data, together with previous work [34, 37], support that the Ctf8 and Dcc1 subunits of CTF18, forming the regulatory module interacting with Pol ε [37], are flexibly tethered to the RFC-module via binding to the Ctf18 C-terminus, which is separated by the N-terminal RFC1-like module of Ctf18 by ~90 amino acid flexible linker. Therefore,

CTF18 comprises two structurally distinct modules that cooperate to load PCNA onto the leading strand, facilitating replication by Pol ε.

The CTF18-PCNA complex was observed in an autoinhibited conformation, which prevents DNA binding. This mirrors the similar conformation seen in hRFC and scRFC, as previously reported [10, 11]. Such conformation represents a transient encounter complex that occurs early in the clamp loading process, before the opening of the clamp. We demonstrate a striking architectural conservation between the CTF18 complex and the canonical human RFC complex [10], despite the variations in the large RFC subunit in the two assemblies. Specifically, CTF18 utilizes three subunits (Ctf18, RFC2, RFC4 and RFC5) to engage two PCNA protomers. However, the engagement of the third PCNA protomer by RFC3 is necessary to initiate the opening of the PCNA ring interface, a process that requires a conformational shift of the AAA+ pentamer from an autoinhibited to an active state. Supporting this, previous structural studies on scRFC have shown that the conformation of RFC bound to open PCNA is facilitated through a 'crab-claw' mechanism, which is inherently predisposed to DNA binding [11]. This conformational change creates an opening between the A′ segment and the AAA+ module in the A subunit, allowing primer-template DNA to bind within the RFC inner chamber [11] (Figure 4b). Remarkably, this significant conformational shift occurs rapidly [57], does not depend on ATP hydrolysis, and ensures the sequential binding of PCNA and the DNA substrate in the correct order. While our study did not resolve the active conformation of CTF18, the observed structural conservation in the autoinhibited state, particularly of the large CTF18 subunit (Figure 2), suggests that a similar 'crab-claw' mechanism may facilitate the transition of CTF18 to its active state for PCNA opening and DNA binding. This structural

conservation includes the presence of a separation pin in the CTF18 large subunit, analogous to the one that interacts with DNA in the yeast RFC complex [11] (Figure 4e).

The main structural differences between CTF18 and the canonical RFC include increased mobility of the large subunit and the presence of a β-hairpin that attaches to the RFC5 subunit. The enhanced mobility of the large subunit is likely enhanced by the low-affinity PIP motif that anchors it to the PCNA ring. We propose that the β-hairpin may have evolved to counterbalance the mobility of the large subunit, helping to maintain its connection to the RFC pentamer. Additionally, an intriguing possibility is that the β-hairpin operates through a 'flying cast' mechanism, keeping the CTF18 large subunit near the RFC pentamer even when the RFC2/3/4/5 subunits are engaged with RFC1 of the canonical RFC (Figure 6). This arrangement could provide a mechanism for recycling the RFC2/3/4/5 subunits and, following the detachment of RFC1, allow rapid assembly of the CTF18 pentamer for loading PCNA onto the leading strand. Further structural and functional studies are needed to further investigate this hypothesis.

Figures

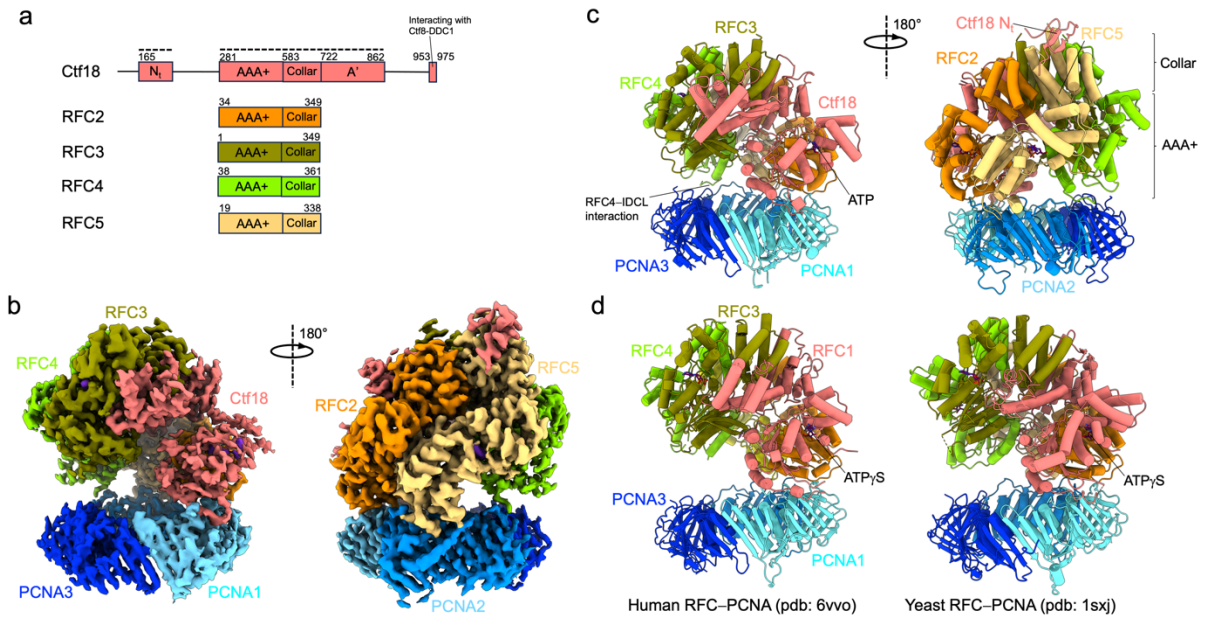

Figure 1. ***Cryo-EM structure of the human CTF18-PCNA complex in the presence of ATP.*** **a)** Domain organization of the CTF18 subunits forming the RFC pentamer. The dotted line above the Ctf18 subunit highlights the regions that are observed in the cryo-EM map. **b)** Two views of the Cryo-EM map of the CTF18–PCNA complex, colored by subunits. The less sharp definition of the map region corresponding to the AAA+ domain of the Ctf18 subunit supports a relatively high mobility of this subunit. **c)** Molecular model of the CTF18–PCNA complex in ribbon representation. **d)** Structures of the human (left) [10] and *Saccharomyces Cerevisiae* (right) [8] RFC–PCNA complex, which present the RFC pentamer in an auto-inhibited conformation analogous to the one captured in the CTF18–PCNA complex.

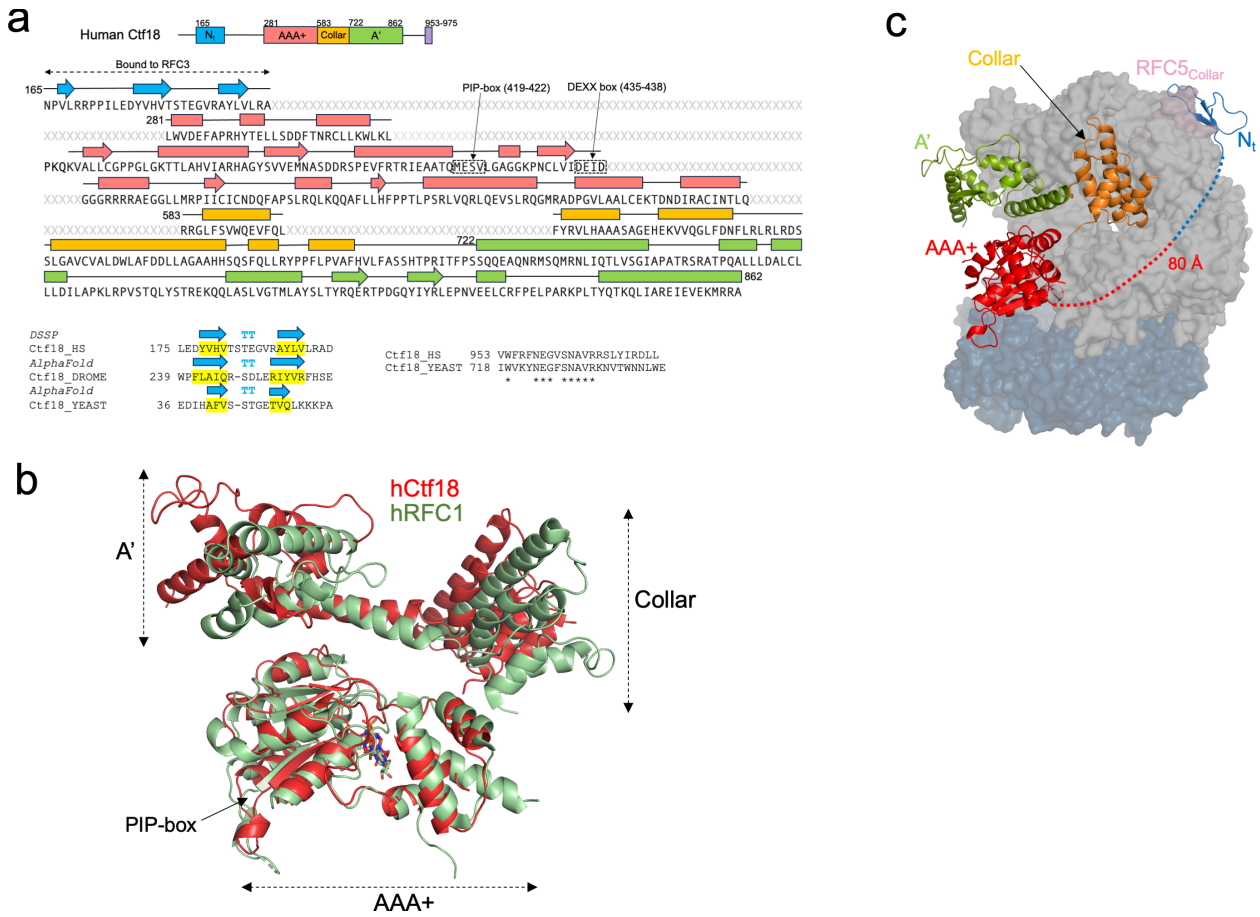

Figure 2. ***Structure of the Ctf18 subunit.*** **a)** Sequence of the human Ctf18 subunit, highlighting the secondary structural elements as assigned in the cryo-EM model. The atypical PCNA-interacting motif (PIP-box) and conserved DEXX box are boxed. Below the Ctf18 sequence to the left, the sequences of the N-terminus of human and other lower eukaryotes Ctf18, together with the secondary prediction by AlphaFold [50] are shown, highlighting the conservation of the β-hairpin fold. Below the Ctf18 sequence to the right, the alignment of the C-terminal region of human and *Saccharomyces Cerevisiae* Ctf18, which interacts with the Ctf8/DCC1 subunits, is shown. Asterisks denote conserved residues. **b)** Superposition of the human Ctf18 and RFC1 (PDB: 6vvo [10]) subunit structures, with subdomains labeled. **c)** Structure of the Ctf18 subunit, in ribbon

representation, within the CTF18–PCNA complex. The Ctf18 subdomains are colored-coded as in panel **(a)**. The other complex subunits are shown as surfaces.

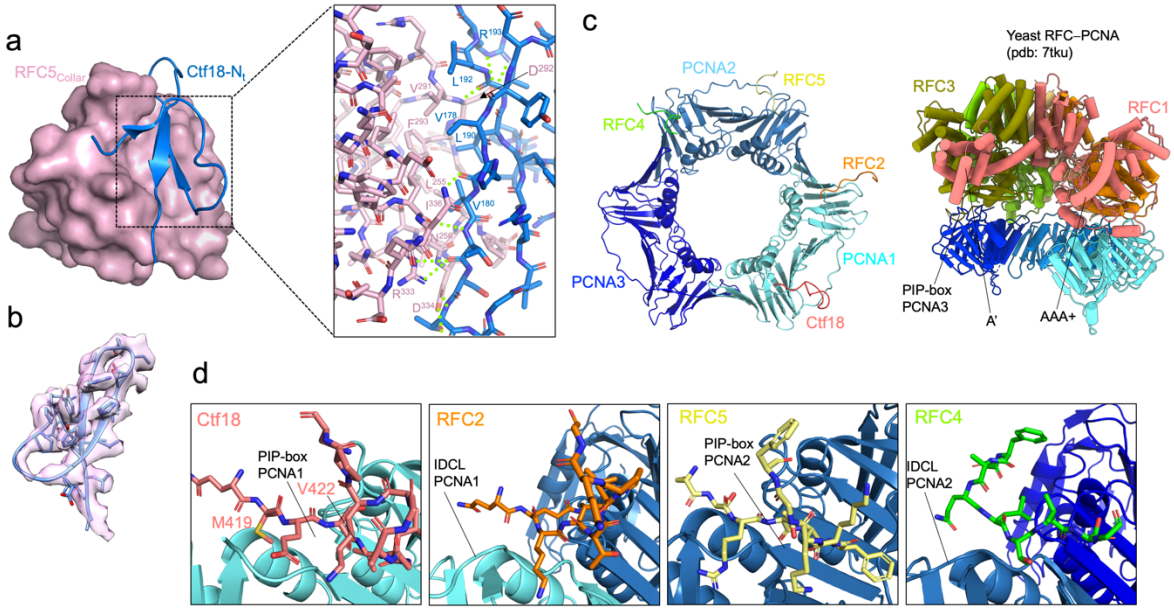

Figure 3. ***Structural details of the Ctf18-RFC3 and CTF18-PCNA interactions.*** **a)** Model of the RFC3 collar domain and Ctf18 N-terminal β-hairpin, in surface and ribbon representation, respectively. The inset shows the interface in stick representation, with hydrogen bonds shown as green dotted lines. **b)** Map region around the Ctf18 N-terminal β-hairpin. **c)** Model of the PCNA homotrimer bound to the four CTF18 interacting regions. To the right, the structure of the yeast RFC–PCNA complex [11] with an open clamp, highlighting the engagement of all five RFC subunits to PCNA, required for clamp opening. **d)** Model of the regions of the CTF18–PCNA interactions, with CTF18 subunit residues shown as sticks and PCNA as ribbon.

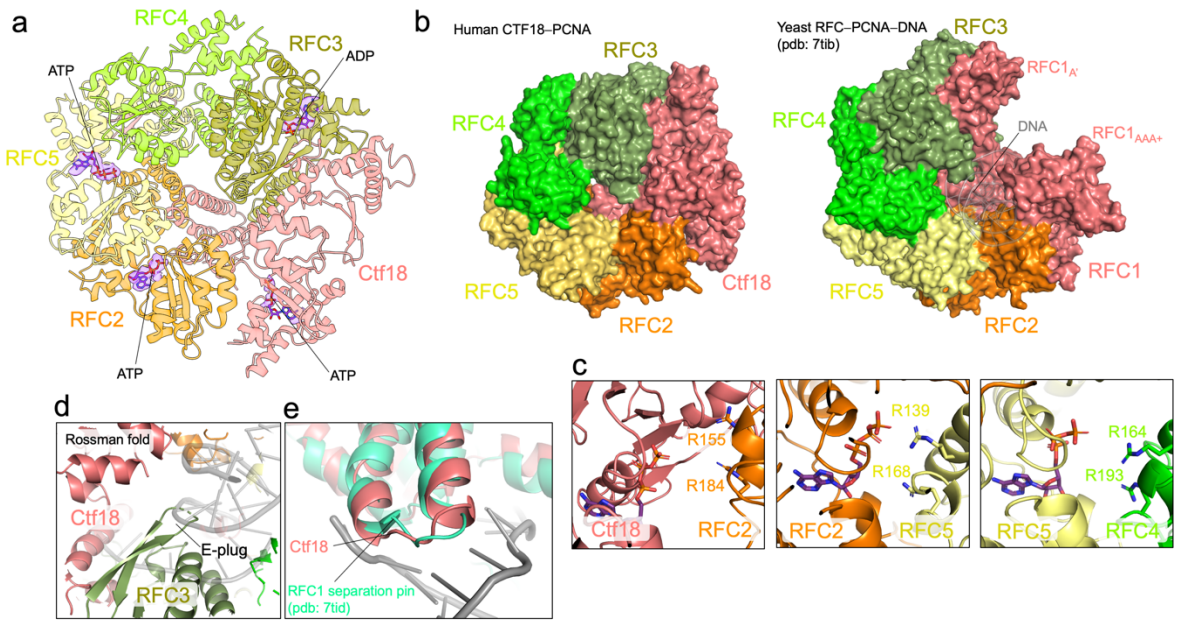

Figure 4. ***Analysis of the auto-inhibited conformation of the CTF18 pentamer and nucleotide coordination*. a)** Ribbon model of the CTF18 pentamer (PCNA hidden). Nucleotide molecules are shown as sticks, with the corresponding cryo-EM density. **b)** Surface representation of (left) the CTF18 pentamer and (right) the yeast RFC pentamer bound to open PCNA and primer-template DNA [11]. PCNA is hidden in both structures. The overtwisted CTF18 pentamer cannot accommodate DNA within the inner chamber. **c)** Model of the ATP active sites in the CTF18–PCNA complex, showing disruption of the interactions mediated by the arginine fingers. **d)** Detail of the inner chamber region of the CTF18 pentamer, showing the β-hairpin (E-plug) of RFC5 protruding in the region predicted to be occupied by DNA. The DNA (grey ribbon) is modeled as in the yeast RFC–DNA–PCNA complex [11]. **e)** The structures of the RFC1 subunit of the RFC–DNA–PCNA complex [11] and the Ctf18 subunit of the CTF18–PCNA complex are aligned to highlight the conservation of the separation pin interacting with DNA.

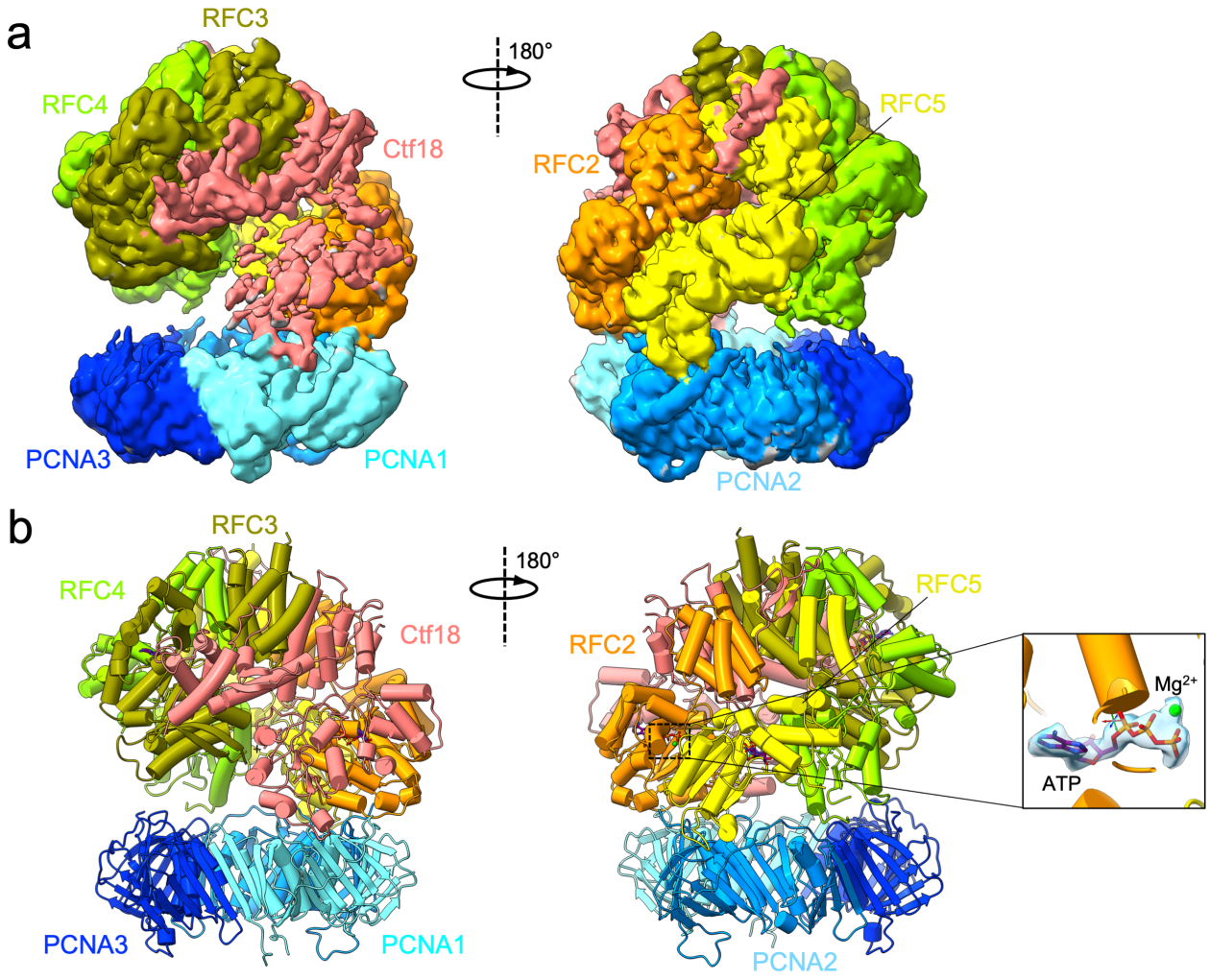

Figure 5. ***Cryo-EM structure of the human CTF18-PCNA complex in the presence of ATP and Mg^{2+}.*** **a)** Two views of the Cryo-EM map, colored by subunits. **b)** Molecular model in ribbon representation. The inset shows map and model of the ATP molecule bound to the RFC2 subunit, with a discernible Mg^{2+} atom.

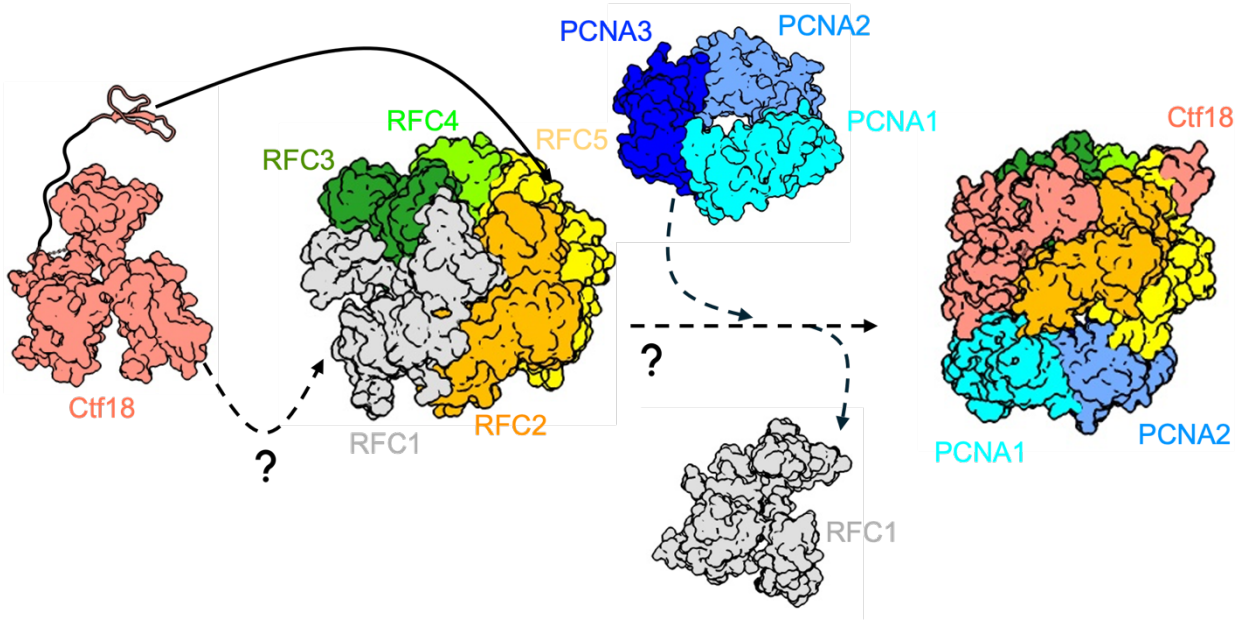

Figure 6. ***Model of the proposed 'flying cast' mechanism for recruiting the Ctf18 large subunit of CTF18 to the RFC pentamer.*** The N-terminal β-hairpin of Ctf18 engages the RFC5 subunit within the RFC pentamer, displacing the RFC1 subunit and thereby recycling the RFC2/3/4/5 subunits.

Data Availability

The maps of Ctf18-RFC-ATP-PCNA and Ctf18-RFC-ATP-Mg^{2+}-PCNA complexes have been deposited in the EMBD with accession codes EMD-XXX, and EMD-XXX and the atomic models in the Protein Data Bank under accession codes PDB XXX and PDB XXX.

References

1. Hubscher U, Maga G, Spadari S. Eukaryotic DNA polymerases. Annu Rev Biochem. 2002;71:133-63. Epub 2002/06/05. doi: 10.1146/annurev.biochem.71.090501.150041. PubMed PMID: 12045093.
2. Choe KN, Moldovan GL. Forging Ahead through Darkness: PCNA, Still the Principal Conductor at the Replication Fork. Mol Cell. 2017;65(3):380-92. Epub 2017/02/06. doi:

10.1016/j.molcel.2016.12.020. PubMed PMID: 28157503; PubMed Central PMCID: PMCPMC5302417.
3. Moldovan GL, Pfander B, Jentsch S. PCNA controls establishment of sister chromatid cohesion during S phase. Mol Cell. 2006;23(5):723-32. Epub 2006/08/29. doi: 10.1016/j.molcel.2006.07.007. PubMed PMID: 16934511.
4. Indiani C, O'Donnell M. The replication clamp-loading machine at work in the three domains of life. Nat Rev Mol Cell Biol. 2006;7(10):751-61. Epub 2006/09/07. doi: 10.1038/nrm2022. PubMed PMID: 16955075.
5. Kelch BA, Makino DL, O'Donnell M, Kuriyan J. Clamp loader ATPases and the evolution of DNA replication machinery. BMC Biol. 2012;10:34. Epub 2012/04/24. doi: 10.1186/1741-7007-10-34. PubMed PMID: 22520345; PubMed Central PMCID: PMCPMC3331839.
6. Kang MS, Ryu E, Lee SW, Park J, Ha NY, Ra JS, et al. Regulation of PCNA cycling on replicating DNA by RFC and RFC-like complexes. Nat Commun. 2019;10(1):2420. Epub 2019/06/05. doi: 10.1038/s41467-019-10376-w. PubMed PMID: 31160570; PubMed Central PMCID: PMCPMC6546911.
7. Jeruzalmi D, O'Donnell M, Kuriyan J. Crystal structure of the processivity clamp loader gamma (gamma) complex of E. coli DNA polymerase III. Cell. 2001;106(4):429-41. Epub 2001/08/30. doi: 10.1016/s0092-8674(01)00463-9. PubMed PMID: 11525729.
8. Bowman GD, O'Donnell M, Kuriyan J. Structural analysis of a eukaryotic sliding DNA clamp-clamp loader complex. Nature. 2004;429(6993):724-30. Epub 2004/06/18. doi: 10.1038/nature02585. PubMed PMID: 15201901.
9. Kazmirski SL, Podobnik M, Weitze TF, O'Donnell M, Kuriyan J. Structural analysis of the inactive state of the Escherichia coli DNA polymerase clamp-loader complex. Proc Natl Acad Sci U S A. 2004;101(48):16750-5. Epub 2004/11/24. doi: 10.1073/pnas.0407904101. PubMed PMID: 15556993; PubMed Central PMCID: PMCPMC529418.
10. Gaubitz C, Liu X, Magrino J, Stone NP, Landeck J, Hedglin M, et al. Structure of the human clamp loader reveals an autoinhibited conformation of a substrate-bound AAA+ switch. Proc Natl Acad Sci U S A. 2020;117(38):23571-80. Epub 2020/09/11. doi: 10.1073/pnas.2007437117. PubMed PMID: 32907938; PubMed Central PMCID: PMCPMC7519235.
11. Gaubitz C, Liu X, Pajak J, Stone NP, Hayes JA, Demo G, et al. Cryo-EM structures reveal high-resolution mechanism of a DNA polymerase sliding clamp loader. Elife. 2022;11. Epub 2022/02/19. doi: 10.7554/eLife.74175. PubMed PMID: 35179493; PubMed Central PMCID: PMCPMC8893722.
12. Schrecker M, Castaneda JC, Devbhandari S, Kumar C, Remus D, Hite RK. Multistep loading of a DNA sliding clamp onto DNA by replication factor C. Elife. 2022;11. Epub 2022/08/09. doi: 10.7554/eLife.78253. PubMed PMID: 35939393; PubMed Central PMCID: PMCPMC9359705.
13. Turner J, Hingorani MM, Kelman Z, O'Donnell M. The internal workings of a DNA polymerase clamp-loading machine. EMBO J. 1999;18(3):771-83. Epub 1999/02/02. doi: 10.1093/emboj/18.3.771. PubMed PMID: 9927437; PubMed Central PMCID: PMCPMC1171170.
14. Gomes XV, Schmidt SL, Burgers PM. ATP utilization by yeast replication factor C. II. Multiple stepwise ATP binding events are required to load proliferating cell nuclear antigen onto primed DNA. J Biol Chem. 2001;276(37):34776-83. Epub 2001/07/04. doi: 10.1074/jbc.M011743200. PubMed PMID: 11432856.

15. Chen S, Levin MK, Sakato M, Zhou Y, Hingorani MM. Mechanism of ATP-driven PCNA clamp loading by S. cerevisiae RFC. J Mol Biol. 2009;388(3):431-42. Epub 2009/03/17. doi: 10.1016/j.jmb.2009.03.014. PubMed PMID: 19285992; PubMed Central PMCID: PMCPMC2700029.
16. Simonetta KR, Kazmirski SL, Goedken ER, Cantor AJ, Kelch BA, McNally R, et al. The mechanism of ATP-dependent primer-template recognition by a clamp loader complex. Cell. 2009;137(4):659-71. Epub 2009/05/20. doi: 10.1016/j.cell.2009.03.044. PubMed PMID: 19450514; PubMed Central PMCID: PMCPMC2684988.
17. Kelch BA, Makino DL, O'Donnell M, Kuriyan J. How a DNA polymerase clamp loader opens a sliding clamp. Science. 2011;334(6063):1675-80. Epub 2011/12/24. doi: 10.1126/science.1211884. PubMed PMID: 22194570; PubMed Central PMCID: PMCPMC3281585.
18. Kelch BA. Review: The lord of the rings: Structure and mechanism of the sliding clamp loader. Biopolymers. 2016;105(8):532-46. Epub 2016/02/27. doi: 10.1002/bip.22827. PubMed PMID: 26918303.
19. Jeruzalmi D, O'Donnell M, Kuriyan J. Clamp loaders and sliding clamps. Curr Opin Struct Biol. 2002;12(2):217-24. Epub 2002/04/18. doi: 10.1016/s0959-440x(02)00313-5. PubMed PMID: 11959500.
20. Lee KY, Park SH. Eukaryotic clamp loaders and unloaders in the maintenance of genome stability. Exp Mol Med. 2020;52(12):1948-58. Epub 2020/12/20. doi: 10.1038/s12276-020-00533-3. PubMed PMID: 33339954; PubMed Central PMCID: PMCPMC8080817.
21. Mayer ML, Gygi SP, Aebersold R, Hieter P. Identification of RFC(Ctf18p, Ctf8p, Dcc1p): an alternative RFC complex required for sister chromatid cohesion in S. cerevisiae. Mol Cell. 2001;7(5):959-70. Epub 2001/06/08. doi: 10.1016/s1097-2765(01)00254-4. PubMed PMID: 11389843.
22. Naiki T, Kondo T, Nakada D, Matsumoto K, Sugimoto K. Chl12 (Ctf18) forms a novel replication factor C-related complex and functions redundantly with Rad24 in the DNA replication checkpoint pathway. Mol Cell Biol. 2001;21(17):5838-45. Epub 2001/08/04. doi: 10.1128/MCB.21.17.5838-5845.2001. PubMed PMID: 11486023; PubMed Central PMCID: PMCPMC87303.
23. Bylund GO, Burgers PM. Replication protein A-directed unloading of PCNA by the Ctf18 cohesion establishment complex. Mol Cell Biol. 2005;25(13):5445-55. Epub 2005/06/21. doi: 10.1128/MCB.25.13.5445-5455.2005. PubMed PMID: 15964801; PubMed Central PMCID: PMCPMC1156988.
24. Crabbe L, Thomas A, Pantesco V, De Vos J, Pasero P, Lengronne A. Analysis of replication profiles reveals key role of RFC-Ctf18 in yeast replication stress response. Nat Struct Mol Biol. 2010;17(11):1391-7. Epub 2010/10/26. doi: 10.1038/nsmb.1932. PubMed PMID: 20972444.
25. Liu HW, Bouchoux C, Panarotto M, Kakui Y, Patel H, Uhlmann F. Division of Labor between PCNA Loaders in DNA Replication and Sister Chromatid Cohesion Establishment. Mol Cell. 2020;78(4):725-38 e4. Epub 2020/04/12. doi: 10.1016/j.molcel.2020.03.017. PubMed PMID: 32277910; PubMed Central PMCID: PMCPMC7242910.
26. al-Khodairy F, Carr AM. DNA repair mutants defining G2 checkpoint pathways in Schizosaccharomyces pombe. EMBO J. 1992;11(4):1343-50. Epub 1992/04/01. doi:

10.1002/j.1460-2075.1992.tb05179.x. PubMed PMID: 1563350; PubMed Central PMCID: PMCPMC556583.
27. Kim J, Robertson K, Mylonas KJ, Gray FC, Charapitsa I, MacNeill SA. Contrasting effects of Elg1-RFC and Ctf18-RFC inactivation in the absence of fully functional RFC in fission yeast. Nucleic Acids Res. 2005;33(13):4078-89. Epub 2005/07/26. doi: 10.1093/nar/gki728. PubMed PMID: 16040599; PubMed Central PMCID: PMCPMC1179736.
28. Bermudez VP, Lindsey-Boltz LA, Cesare AJ, Maniwa Y, Griffith JD, Hurwitz J, et al. Loading of the human 9-1-1 checkpoint complex onto DNA by the checkpoint clamp loader hRad17-replication factor C complex in vitro. Proc Natl Acad Sci U S A. 2003;100(4):1633-8. Epub 2003/02/13. doi: 10.1073/pnas.0437927100. PubMed PMID: 12578958; PubMed Central PMCID: PMCPMC149884.
29. Terret ME, Sherwood R, Rahman S, Qin J, Jallepalli PV. Cohesin acetylation speeds the replication fork. Nature. 2009;462(7270):231-4. Epub 2009/11/13. doi: 10.1038/nature08550. PubMed PMID: 19907496; PubMed Central PMCID: PMCPMC2777716.
30. Zhang J, Shi X, Li Y, Kim BJ, Jia J, Huang Z, et al. Acetylation of Smc3 by Eco1 is required for S phase sister chromatid cohesion in both human and yeast. Mol Cell. 2008;31(1):143-51. Epub 2008/07/11. doi: 10.1016/j.molcel.2008.06.006. PubMed PMID: 18614053.
31. Rolef Ben-Shahar T, Heeger S, Lehane C, East P, Flynn H, Skehel M, et al. Eco1-dependent cohesin acetylation during establishment of sister chromatid cohesion. Science. 2008;321(5888):563-6. Epub 2008/07/26. doi: 10.1126/science.1157774. PubMed PMID: 18653893.
32. Unal E, Heidinger-Pauli JM, Kim W, Guacci V, Onn I, Gygi SP, et al. A molecular determinant for the establishment of sister chromatid cohesion. Science. 2008;321(5888):566-9. Epub 2008/07/26. doi: 10.1126/science.1157880. PubMed PMID: 18653894.
33. Kubota T, Nishimura K, Kanemaki MT, Donaldson AD. The Elg1 replication factor C-like complex functions in PCNA unloading during DNA replication. Mol Cell. 2013;50(2):273-80. Epub 2013/03/19. doi: 10.1016/j.molcel.2013.02.012. PubMed PMID: 23499004.
34. Stokes K, Winczura A, Song B, Piccoli G, Grabarczyk DB. Ctf18-RFC and DNA Pol ϵ form a stable leading strand polymerase/clamp loader complex required for normal and perturbed DNA replication. Nucleic Acids Res. 2020;48(14):8128-45. Epub 2020/06/26. doi: 10.1093/nar/gkaa541. PubMed PMID: 32585006; PubMed Central PMCID: PMCPMC7641331.
35. Bermudez VP, Maniwa Y, Tappin I, Ozato K, Yokomori K, Hurwitz J. The alternative Ctf18-Dcc1-Ctf8-replication factor C complex required for sister chromatid cohesion loads proliferating cell nuclear antigen onto DNA. Proc Natl Acad Sci U S A. 2003;100(18):10237-42. Epub 2003/08/22. doi: 10.1073/pnas.1434308100. PubMed PMID: 12930902; PubMed Central PMCID: PMCPMC193545.
36. Fujisawa R, Ohashi E, Hirota K, Tsurimoto T. Human CTF18-RFC clamp-loader complexed with non-synthesising DNA polymerase epsilon efficiently loads the PCNA sliding clamp. Nucleic Acids Res. 2017;45(8):4550-63. Epub 2017/02/16. doi: 10.1093/nar/gkx096. PubMed PMID: 28199690; PubMed Central PMCID: PMCPMC5416766.
37. Grabarczyk DB, Silkenat S, Kisker C. Structural Basis for the Recruitment of Ctf18-RFC to the Replisome. Structure. 2018;26(1):137-44 e3. Epub 2017/12/12. doi: 10.1016/j.str.2017.11.004. PubMed PMID: 29225079.

38. Jones ML, Baris Y, Taylor MRG, Yeeles JTP. Structure of a human replisome shows the organisation and interactions of a DNA replication machine. EMBO J. 2021;40(23):e108819. Epub 2021/10/26. doi: 10.15252/embj.2021108819. PubMed PMID: 34694004; PubMed Central PMCID: PMCPMC8634136.
39. Langston LD, Zhang D, Yurieva O, Georgescu RE, Finkelstein J, Yao NY, et al. CMG helicase and DNA polymerase epsilon form a functional 15-subunit holoenzyme for eukaryotic leading-strand DNA replication. Proc Natl Acad Sci U S A. 2014;111(43):15390-5. Epub 2014/10/15. doi: 10.1073/pnas.1418334111. PubMed PMID: 25313033; PubMed Central PMCID: PMCPMC4217400.
40. Yeeles JTP, Janska A, Early A, Diffley JFX. How the Eukaryotic Replisome Achieves Rapid and Efficient DNA Replication. Mol Cell. 2017;65(1):105-16. Epub 2016/12/19. doi: 10.1016/j.molcel.2016.11.017. PubMed PMID: 27989442; PubMed Central PMCID: PMCPMC5222725.
41. Chilkova O, Stenlund P, Isoz I, Stith CM, Grabowski P, Lundstrom EB, et al. The eukaryotic leading and lagging strand DNA polymerases are loaded onto primer-ends via separate mechanisms but have comparable processivity in the presence of PCNA. Nucleic Acids Res. 2007;35(19):6588-97. Epub 2007/10/02. doi: 10.1093/nar/gkm741. PubMed PMID: 17905813; PubMed Central PMCID: PMCPMC2095795.
42. Zheng SQ, Palovcak E, Armache JP, Verba KA, Cheng Y, Agard DA. MotionCor2: anisotropic correction of beam-induced motion for improved cryo-electron microscopy. Nat Methods. 2017;14(4):331-2. Epub 2017/03/03. doi: 10.1038/nmeth.4193. PubMed PMID: 28250466; PubMed Central PMCID: PMCPMC5494038.
43. Rohou A, Grigorieff N. CTFFIND4: Fast and accurate defocus estimation from electron micrographs. J Struct Biol. 2015;192(2):216-21. Epub 2015/08/19. doi: 10.1016/j.jsb.2015.08.008. PubMed PMID: 26278980; PubMed Central PMCID: PMCPMC6760662.
44. Kimanius D, Dong L, Sharov G, Nakane T, Scheres SHW. New tools for automated cryo-EM single-particle analysis in RELION-4.0. Biochem J. 2021;478(24):4169-85. Epub 2021/11/17. doi: 10.1042/BCJ20210708. PubMed PMID: 34783343; PubMed Central PMCID: PMCPMC8786306.
45. Bepler T, Morin A, Rapp M, Brasch J, Shapiro L, Noble AJ, et al. Positive-unlabeled convolutional neural networks for particle picking in cryo-electron micrographs. Nat Methods. 2019;16(11):1153-60. Epub 2019/10/09. doi: 10.1038/s41592-019-0575-8. PubMed PMID: 31591578; PubMed Central PMCID: PMCPMC6858545.
46. Kelley LA, Mezulis S, Yates CM, Wass MN, Sternberg MJ. The Phyre2 web portal for protein modeling, prediction and analysis. Nat Protoc. 2015;10(6):845-58. Epub 2015/05/08. doi: 10.1038/nprot.2015.053. PubMed PMID: 25950237; PubMed Central PMCID: PMCPMC5298202.
47. Emsley P, Lohkamp B, Scott WG, Cowtan K. Features and development of Coot. Acta Crystallogr D Biol Crystallogr. 2010;66(Pt 4):486-501. Epub 2010/04/13. doi: 10.1107/S0907444910007493. PubMed PMID: 20383002; PubMed Central PMCID: PMCPMC2852313.
48. Croll TI. ISOLDE: a physically realistic environment for model building into low-resolution electron-density maps. Acta Crystallogr D Struct Biol. 2018;74(Pt 6):519-30. Epub 2018/06/07. doi: 10.1107/S2059798318002425. PubMed PMID: 29872003; PubMed Central PMCID: PMCPMC6096486.

49. Adams PD, Afonine PV, Bunkoczi G, Chen VB, Davis IW, Echols N, et al. PHENIX: a comprehensive Python-based system for macromolecular structure solution. Acta Crystallogr D Biol Crystallogr. 2010;66(Pt 2):213-21. Epub 2010/02/04. doi: 10.1107/S0907444909052925. PubMed PMID: 20124702; PubMed Central PMCID: PMCPMC2815670.
50. Jumper J, Evans R, Pritzel A, Green T, Figurnov M, Ronneberger O, et al. Highly accurate protein structure prediction with AlphaFold. Nature. 2021;596(7873):583-9. Epub 2021/07/16. doi: 10.1038/s41586-021-03819-2. PubMed PMID: 34265844; PubMed Central PMCID: PMCPMC8371605 have filed non-provisional patent applications 16/701,070 and PCT/EP2020/084238, and provisional patent applications 63/107,362, 63/118,917, 63/118,918, 63/118,921 and 63/118,919, each in the name of DeepMind Technologies Limited, each pending, relating to machine learning for predicting protein structures. The other authors declare no competing interests.
51. Cai J, Uhlmann F, Gibbs E, Flores-Rozas H, Lee CG, Phillips B, et al. Reconstitution of human replication factor C from its five subunits in baculovirus-infected insect cells. Proc Natl Acad Sci U S A. 1996;93(23):12896-901. Epub 1996/11/12. doi: 10.1073/pnas.93.23.12896. PubMed PMID: 8917516; PubMed Central PMCID: PMCPMC24017.
52. Podust VN, Tiwari N, Ott R, Fanning E. Functional interactions among the subunits of replication factor C potentiate and modulate its ATPase activity. J Biol Chem. 1998;273(21):12935-42. Epub 1998/05/28. doi: 10.1074/jbc.273.21.12935. PubMed PMID: 9582326.
53. Cai J, Yao N, Gibbs E, Finkelstein J, Phillips B, O'Donnell M, et al. ATP hydrolysis catalyzed by human replication factor C requires participation of multiple subunits. Proc Natl Acad Sci U S A. 1998;95(20):11607-12. Epub 1998/09/30. doi: 10.1073/pnas.95.20.11607. PubMed PMID: 9751713; PubMed Central PMCID: PMCPMC21688.
54. Schmidt SL, Gomes XV, Burgers PM. ATP utilization by yeast replication factor C. III. The ATP-binding domains of Rfc2, Rfc3, and Rfc4 are essential for DNA recognition and clamp loading. J Biol Chem. 2001;276(37):34784-91. Epub 2001/07/04. doi: 10.1074/jbc.M011633200. PubMed PMID: 11432854.
55. Seybert A, Wigley DB. Distinct roles for ATP binding and hydrolysis at individual subunits of an archaeal clamp loader. EMBO J. 2004;23(6):1360-71. Epub 2004/03/12. doi: 10.1038/sj.emboj.7600130. PubMed PMID: 15014449; PubMed Central PMCID: PMCPMC381406.
56. Sakato M, O'Donnell M, Hingorani MM. A central swivel point in the RFC clamp loader controls PCNA opening and loading on DNA. J Mol Biol. 2012;416(2):163-75. Epub 2011/12/27. doi: 10.1016/j.jmb.2011.12.017. PubMed PMID: 22197374; PubMed Central PMCID: PMCPMC3269524.
57. Liu J, Zhou Y, Hingorani MM. Linchpin DNA-binding residues serve as go/no-go controls in the replication factor C-catalyzed clamp-loading mechanism. J Biol Chem. 2017;292(38):15892-906. Epub 2017/08/16. doi: 10.1074/jbc.M117.798702. PubMed PMID: 28808059; PubMed Central PMCID: PMCPMC5612119.

Supplementary Information

Structure of the human CTF18 clamp loader bound to PCNA

Briola G. R. *et al*

Includes:

Supplementary Figures 1-6

Supplementary Table 1

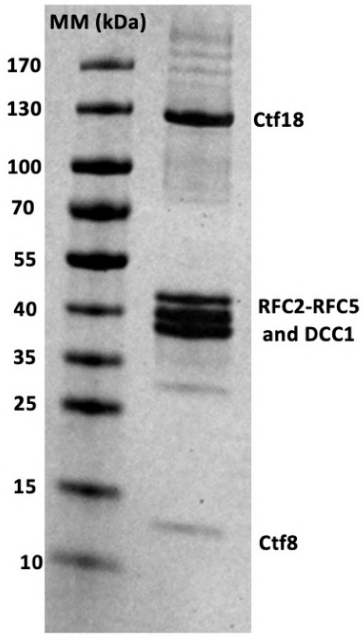

Supplementary Figure 1. *SDS-PAGE gel (4-20%) of the purified human clamp loader CTF18*. Bands corresponding to the different subunits are labeled. The molecular weight standard is shown.

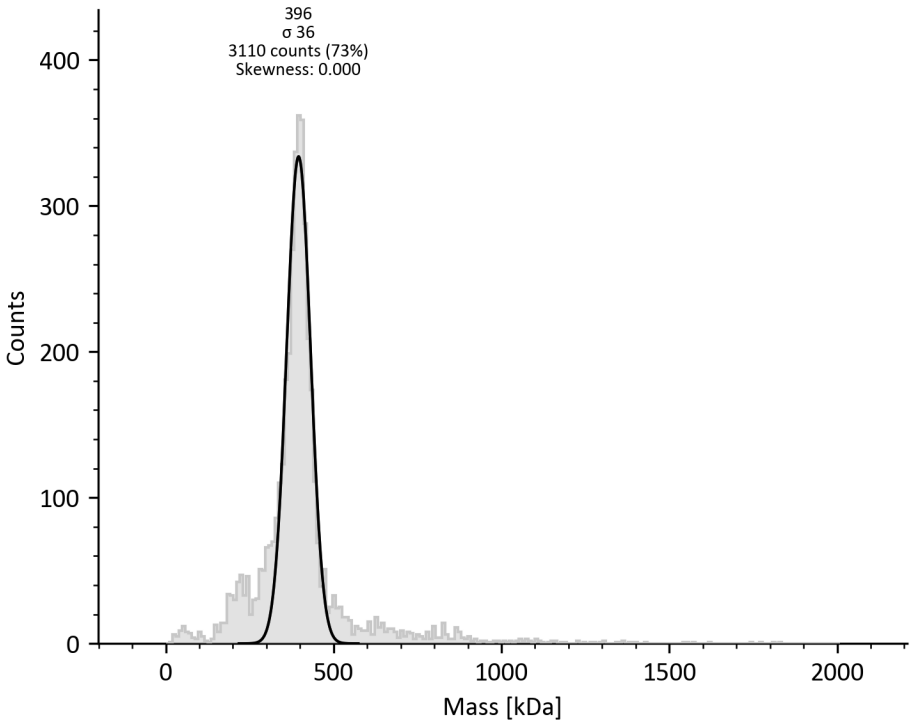

Supplementary Figure 2. *Mass photometry of the purified CTF18 complex*. The histogram of the mass distribution of 50 nM CTF18 in PBS is shown. The expected mass is 324 kDa, while the estimated mass is 396 ± 36 kDa.

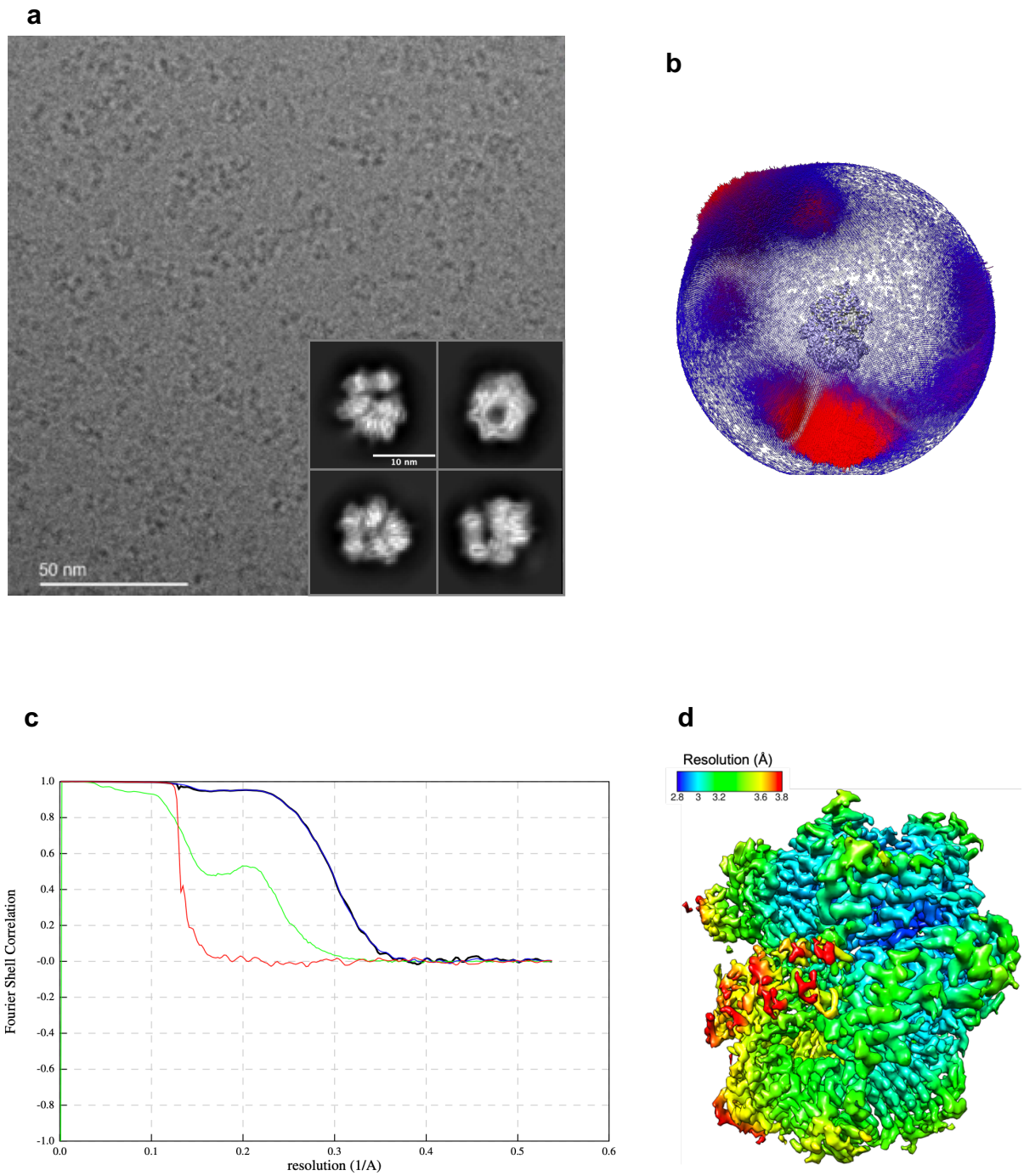

Supplementary Figure 3. *Cryo-EM of the CTF18–PCNA complex in the presence of ATP.* **a)** Representative electron micrograph acquired on a Falcon 4i electron detector in counting mode, and representative 2D class averages. **b)** Angular distributions of projections. **c)** Gold-standard Fourier shell correlation for the reconstruction of the full complex after focused refinement, and resolution estimation using the 0.143 criterion. **d)** Cryo-EM map of the complex, color-coded by local resolution.

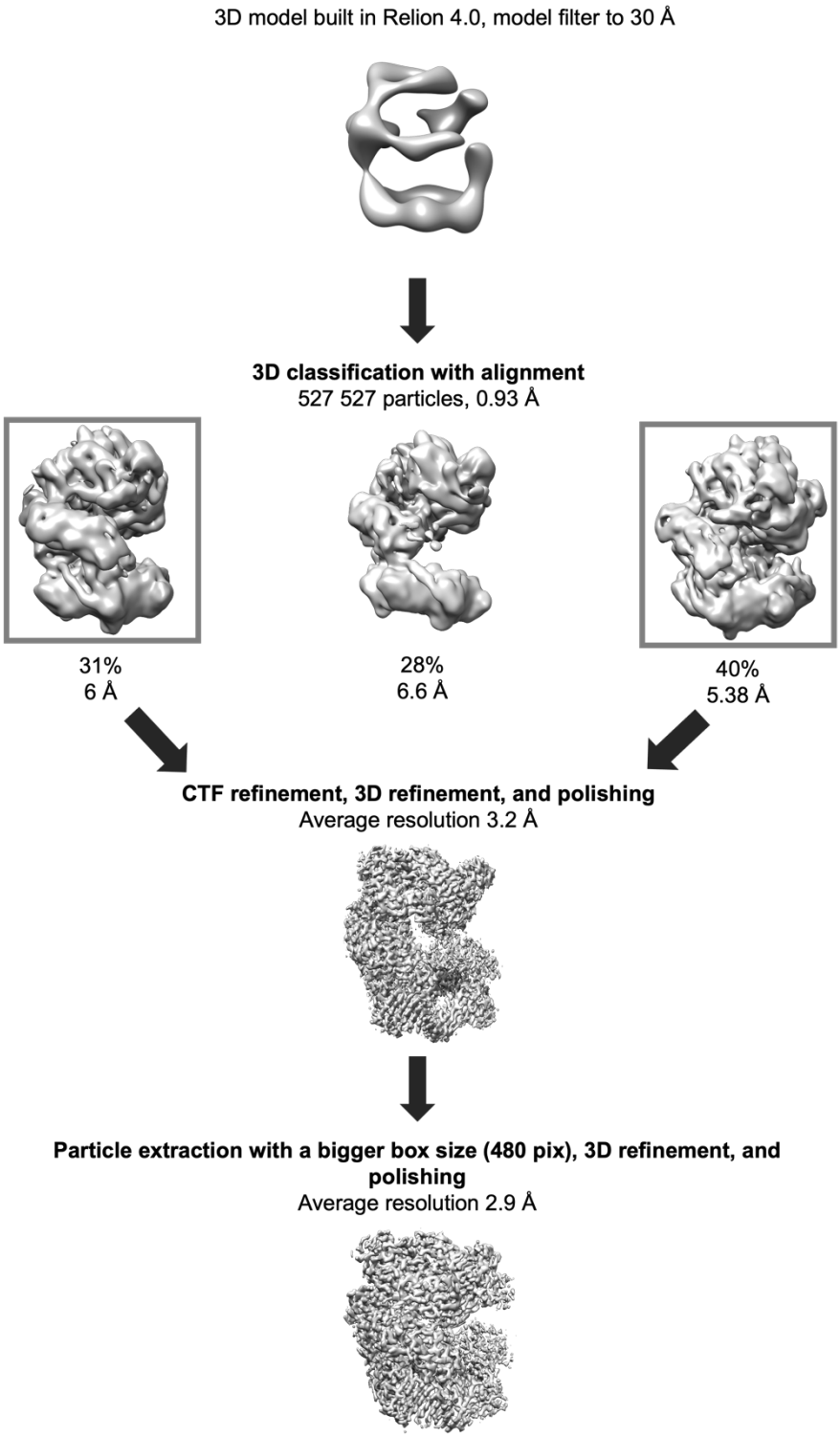

Supplementary Figure 4. Workflow of cryo-EM image processing and 3D reconstruction of Ctf18-RFC-PCNA complex in the presence of 0.5 mM ATP and without Mg^{2+} (Dataset 1). Relion 4.0 was used for image processing and 3D reconstruction.

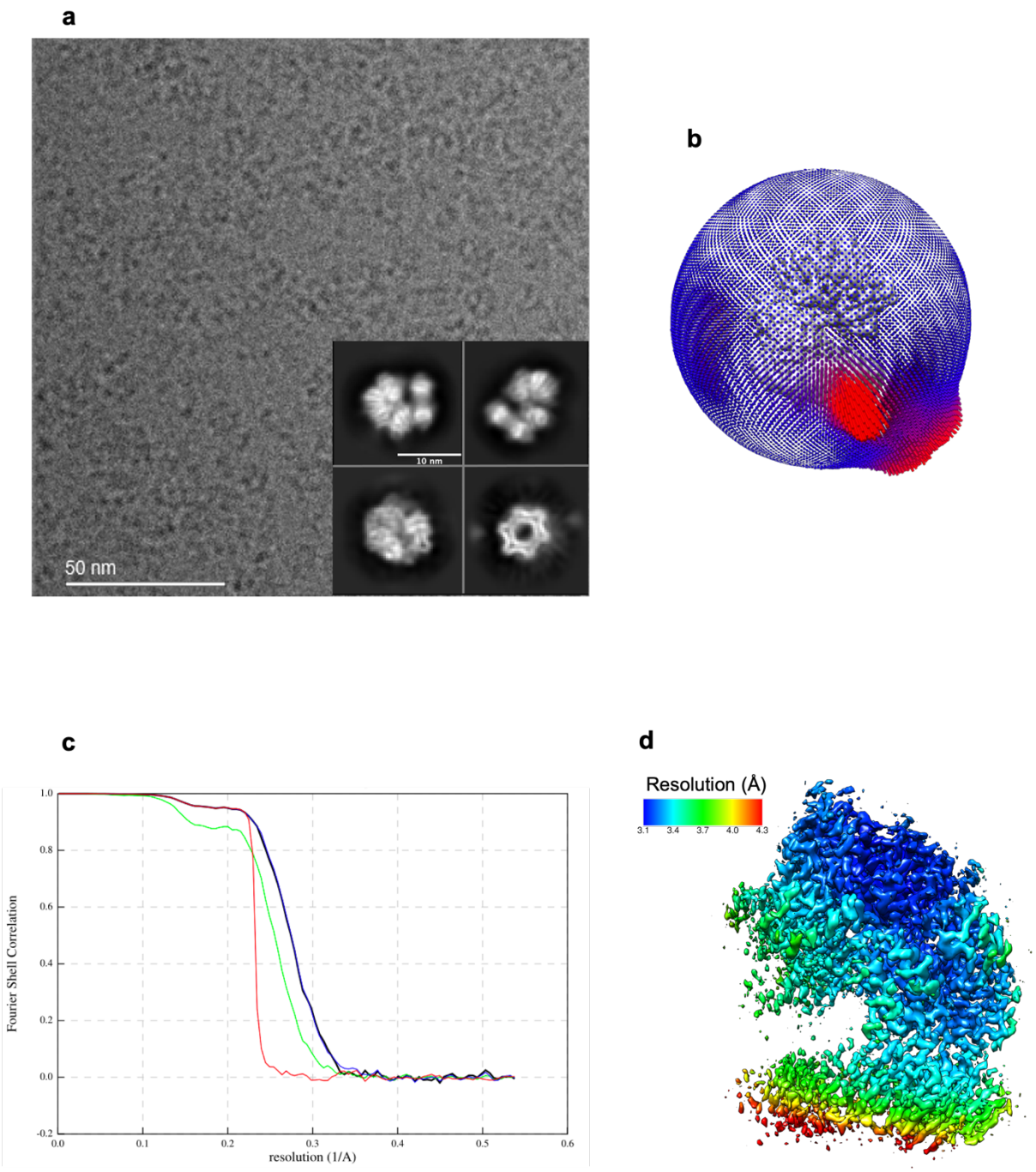

Supplementary Figure 5. a) Cryo-EM of Ctf18-RFC with P/T DNA, ATP, Mg^{2+} and PCNA. Electron micrograph acquired on a Falcon 4i electron detector in counting mode, and representative 2D class averages. **b)** Angular distributions of projections. **c)** Gold-standard Fourier shell correlation for the reconstruction of the full complex after focused refinement, and resolution estimation using the 0.143 criterion. **d)** Cryo-EM map of the complex, color-coded by local resolution.

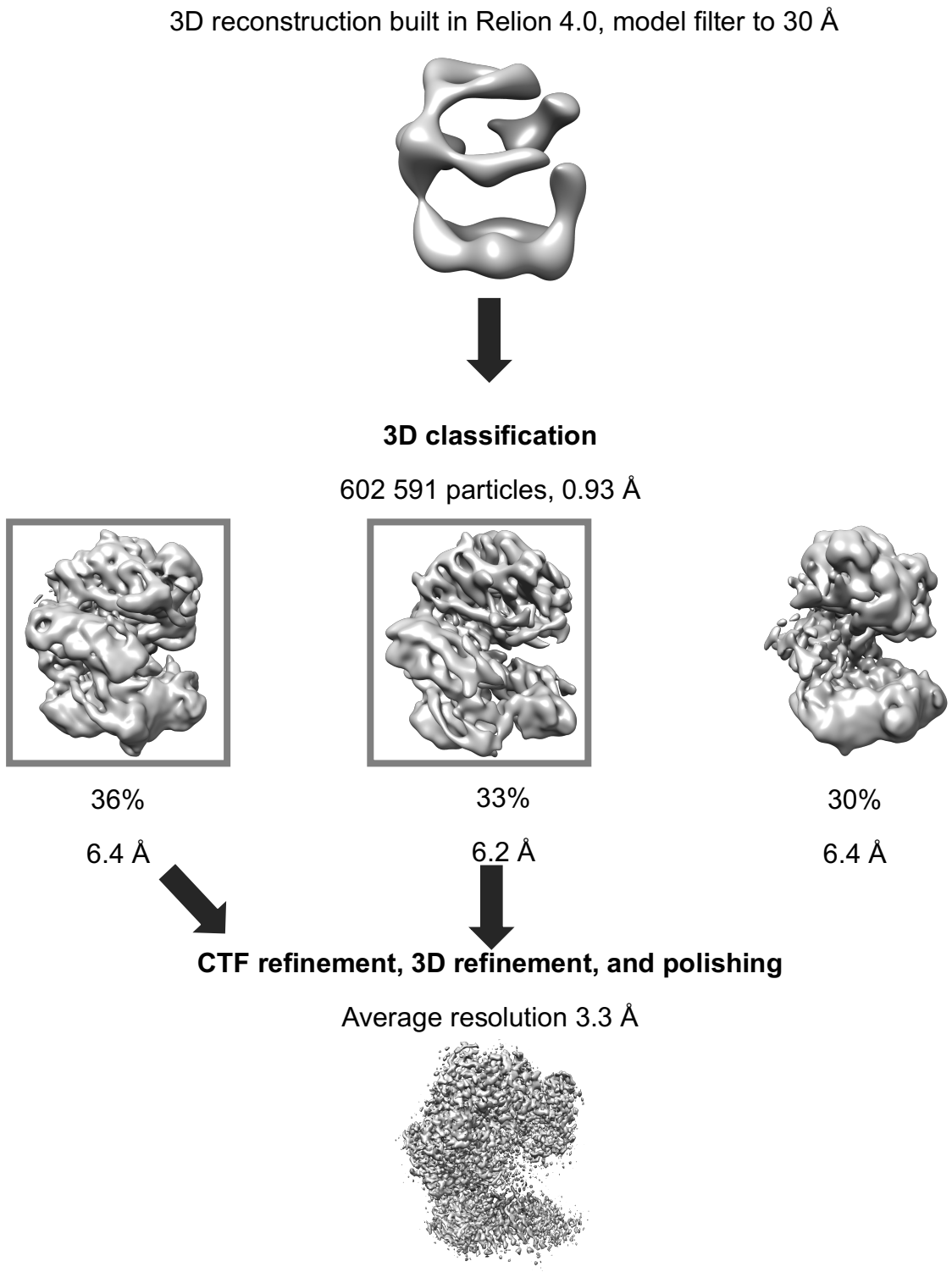

Supplementary Figure 6. Workflow of cryo-EM image processing and 3D reconstruction of Ctf18-RFC-PCNA complex in the presence of 0.5 mM ATP and 5 mM Mg-Acetate (Dataset 2). Relion 4.0 was used for image processing and 3D reconstruction.

	CTF18-PCNA with ATP	CTF18-PCNA with ATP and Mg^{2+}
Data collection and processing		
Magnification	130,000	130,000
Voltage (kV)	300	300
Electron exposure (e–/Å^2)	43	46
Defocus range (μm)	-2.7 to -1.5	-2.7 to -1.5
Pixel size (Å)	0.93	0.93
Symmetry imposed	C1	C1
Initial particle images (no.)	2,043,120	3,216,167
Final particle images (no.)	527,527	602,591
Map resolution (Å)	2.9	3.3
FSC threshold	0.143	0.143
Map resolution range (Å)	2.8-3.8	3.1-4.3
Refinement		
Initial model used (PDB code)	6VVO	6VVO
Model resolution (Å)	3.0	3.5
FSC threshold	0.5	0.5
Map sharpening *B* factor (Å^2)	-67.879	-138.637
Model composition		
Non-hydrogen atoms	19776	19779
Protein residues	2503	2503
Ligands	4	6
B factors (Å^2)		
Protein	69.08	169.79
Ligand	79.49	167.64
R.m.s. deviations		
Bond lengths (Å)	0.005	0.003
Bond angles (°)	0.714	0.547
Validation		
MolProbity score	2.18	2.00
Clashscore	11.53	9.39
Poor rotamers (%)	2.93	2.19
Ramachandran plot		
Favored (%)	96.26	96.38
Allowed (%)	3.66	3.49
Disallowed (%)	0.08	0.12

Supplementary Table 1 Cryo-EM data collection, model refinement, and validation statistics.